Journal of Materials Chemistry A

COMMUNICATION

View Article Online
View Journal | View Issue

Cite this: J. Mater. Chem. A, 2016, 4, 12036

Received 2nd May 2016
Accepted 11th June 2016

DOI: 10.1039/c6ta03669d

www.rsc.org/MaterialsA

The quantum mechanics derived atomistic mechanism underlying the acceleration of catalytic CO oxidation on Pt(110) by surface acoustic waves†

Qi An,[a] Jin Qian,[a] Robert R. Nielsen,[a] Luca Sementa,[b] Giovanni Barcaro,[b] Fabio R. Negreiros,[b] Alessandro Fortunelli[ab] and William A. Goddard III*[a]

Experimental evidence that surface acoustic waves (SAW) can significantly enhance the rate of catalytic oxidation of CO to CO_2 over the Pt(110) catalyst surface [S. Kelling *et al.*, *Faraday Disc.*, 1997, **107**, 435–444] is examined using quantum mechanics (QM) simulations. First we determined the QM based mechanism for the O_2-rich régime of the reaction, and the energy landscape of CO interacting with an O-covered reconstructed Pt(110) surface at both static and dynamic levels, but in the absence of SAW. We then utilized *ab initio* molecular dynamic (AIMD) simulations to determine how SAW might modify the kinetics. We focus here on the short (picosecond time scale) shock spikes induced by switching of domains in the piezoelectric driver on which the catalyst is deposited. We find that SAW-induced spikes promote dynamic changes in the diffusion and desorption, from which we estimate the influence of SAW on CO oxidation rate over Pt(110). We find good agreement with the experimentally observed catalytic enhancement by SAW. With an atomistic mechanism in place one can now consider how to use SAW to enhance other catalytic reactions.

1. Introduction

A great deal of progress has been made in improving catalytic processes through clever use of ligands, surface preparations, solvents, combined with external variables of temperature and pressure. However, major challenges still exist in improving the activity, selectivity and operating conditions for catalytic processes that are of fundamental importance in the energy and environment fields, such as the conversion of petroleum and biomass, water splitting to convert light or fields into energy (H_2), CO_2 reduction to generate fuels, and NH_3 synthesis (Haber–Bosch).[1,2] Alternative, non-conventional approaches exploiting novel external electric, magnetic, or mechanical fields are being investigated to enlarge the parametric space for catalysis.[3,4]

We became particularly interested in several experimental studies reporting promising results of acoustic wave enhanced catalysis (AWEC). One experiment used a 100 nm Pd film deposited on a 1 mm $LiNbO_3$ to generate acoustic waves at the resonant frequencies of the crystal (3.4 MHz, in thickness extension mode or TERO) on the Pd film exposed to a recirculating mixture of ethanol (EtOH) and O_2. The acoustic waves led to accelerated ethanol oxidation to acetaldehyde by 1880-fold with no effect on oxidative dehydrogenation (ODH) to ethene. In contrast, exposing a Pd catalyst to TERO excitation substantially accelerates (by a factor of 6) ethanol decomposition to ethylene (ODH) but has no effect on the rate of acetaldehyde production.[5] No atomistic mechanism has been proposed to explain this puzzling chemistry. Similarly, surface science studies demonstrated that CO oxidation to CO_2 (the COox reaction) over the Pt(110) surface was enhanced sufficiently by surface acoustic waves (SAW) to increase the maximum CO pressure for rapid oxidation by 20%.[6] Again, no atomistically based understanding is available of how SAW can couple to such catalytic processes sufficiently to induce dramatic increases the rates. Thus, there is no guide for identifying which catalytic processes can be accelerated using this new AWEC approach. Indeed altering conditions sometimes leads to no AWEC or even a decrease in the catalytic rates.[7] Clearly to utilize AWEC to design improved catalysts requires an atomistic mechanism to rationalize these experiments.

As a first step in developing an atomistic understanding of how AW might modify rates of catalysis, we chose to examine the effect of SAW on the catalytic oxidation of CO with O_2 on the Pt(110) catalyst surface.[6] COox/Pt(110) has been studied extensively because when CO and O_2 pressures are comparable one observes oscillatory patterns in both space and time (this reaction was the first example of such behavior in the field of heterogeneous catalysis).[8] First we carried out quantum mechanics (QM) computations at the PBE level of Density Function Theory (DFT) to develop an understanding of the

[a]Materials and Process Simulation Center (MSC), California Institute of Technology, Pasadena, CA 91125, USA. E-mail: wag@wag.caltech.edu

[b]CNR-ICCOM and IPCF, Consiglio Nazionale delle Ricerche, via Giuseppe Moruzzi 1, 56124, Pisa, Italy

† Electronic supplementary information (ESI) available: Computational details of DFT and AIMD simulations, illustration of the ReaxFF simulation and an AIMD trajectory as a movie. See DOI: 10.1039/c6ta03669d

underlying reaction mechanisms without SAW. Then we used QM to understand how SAW might increase the COox efficiency. We found good agreement of this new mechanism for AWEC with the surface science experiments.

We consider that homogeneous strain fluctuations at 20 MHz and with wave length of 200 μm are unlikely to affect significantly the COox reaction energy landscape. However, we are aware that flipping the domains in the piezoelectric SAW driver can lead to short (picosecond) shock spikes. Thus we investigated how such shocks propagating to the catalyst surface might couple to diffusion, desorption, and reactive phenomena to modify the rates. We model this phenomenon using *ab initio* molecular dynamics (AIMD) simulations combined with a kinetic model we derived from the QM studies of the COox/Pt(110) reaction. This allows us to estimate the influence of SAW on COox catalytic efficiency. Indeed we find that the predicted SAW enhancement is in good agreement with experiment. This provides an atomistic mechanism that can now be used to design new applications for which SAW might dramatically increase selectivity, produce novel reaction products, or decrease the required temperature or pressure compared to traditional approaches.

2. Computational methodology

We carried out density functional theory (DFT) quantum mechanics using the Perdew–Burke–Ernzerhof (PBE) generalized gradient exchange–correlation (xc) functional,[11] a plane wave basis set, and the projected augmented-wave method to simplify the description of atomic cores.[12] For technical reasons we use two different codes: Quantum Espresso[13] for DFT geometry optimizations and Nudged Elastic Band (NEB)[14] evaluation of energy barriers, and VASP[15] for the AIMD simulations. We validated that the results of the two codes coincide quantitatively for selected static cases.

We found that a kinetic energy cutoff of 500 eV for the plane wave expansions gives excellent convergence of the total energies, energy differences, and structural parameters in structure optimization. The same energy cutoff was applied in both the static DFT and AIMD calculations. The Monkhorst–Pack grid (3 × 3 × 2) in the *k*-space was used in both the DFT and AIMD simulations. For the DFT simulations, our convergence criteria were: a 1×10^{-5} eV energy difference for solving the electronic wave function and 1×10^{-3} eV Å^{-1} force for structure optimization. For the AIMD simulations, our convergence criteria were: a 1×10^{-5} eV energy difference for solving the electronic wave function. The spin-restricted KS solvers were used in the AIMD simulations, and the symmetry was not constrained.

We first optimized the bulk Pt system leading to a lattice parameter of 2.82 Å in agreement with the experimental value of 2.78 Å. Then we created a 3 × 2 supercell along the "*a*" and "*b*" direction and constructed a five layer slab along the *c* direction with 20 Å vacuum. The bottom two Pt layers were fixed during the AIMD simulations. To validate that a 5-layer slab is sufficient, we also calculated the CO absorption energy on the facet sites for a 7-layer slab with 0.83 ML oxygen coverage. The CO absorption energy changed by only 0.01 eV suggesting that the 5-layer slab is sufficient.

The AIMD simulation procedures were as follows. First the systems were heated at a constant rate from 10 to 300 K over 10 ps. Then the systems were equilibrated at 300 K for 1 ps using the NVT (constant volume, constant temperature, and constant number of atoms) ensemble. Next, we heated the system from 300 to 1700 K uniformly over 5 ps. Finally the system was equilibrated at 1700 K for 5 ps before the shock simulations. The time constant for the Nose–Hoover thermostat was 0.1 ps. The time step 1 fs was used for integrating the equation of motion.

To mimic the spikes in the SAW experiments, we introduced a relatively strong shock by displacing the Pt atoms of two bottom layers by 0.5 Å further away from the unfixed layers but keeping them frozen. The intensity of the shock thus may possibly be stronger than that in the SAW experiments but it allows us to observe possible effects of a shock within the short time of a few picoseconds practical for AIMD simulations. This shock increases the potential energy of the supercell typically by 5.5 eV and the temperature of the system by ≈300 K (as shown in Fig. S2 of the ESI†). We applied a microcanonical (NVE) ensemble during the shock simulation. Further computational details are provided in the ESI.†

3. Results and discussion

3.1 Reaction mechanisms without SAW

The experimental apparatus used in ref. 6 is shown in Fig. 1a: an interdigital transducer is composed of a single-crystal piezoelectric film of 1 mm thickness covered on both sides with 500 nm-thick platinum layers exposing the (110) surface. This was obtained by growing Pt on a NaCl substrate, then dissolving the ionic substrate on top of a piezoelectric film to which the Pt layer is cold-welded. This was followed by sputtering and annealing the resulting composite system to obtain the proper surface orientation. In this apparatus, the Pt layers lie perpendicular to the propagation path of the SAW, acting simultaneously as catalysts and as electrodes for generating SAW at the surface of the underlying piezoelectric. The SAW frequency is 18.8 to 19.8 MHz with an applied power up to 1 W. Doppler measurements show that the SAW produces surface oscillations that extend up to 20 nm perpendicular to the catalyst surface[6] with a longitudinal wave length of 200 μm, implying a homogeneous strain of $\sim 10^{-4}$.

The COox reaction in ref. 6 was studied over the temperature range between $T = 387$ and $T = 528$ K, with a constant baseline O_2 pressure $P_{O_2} = 1.2 \times 10^{-7}$ Torr. The CO pressure was increased from zero to $P_{CO} = 8 \times 10^{-8}$ Torr, while the evolving CO_2 pressure (P_{CO_2}) was measured in the presence and absence of SAW excitation, as shown in Fig. 1b. Two COox régimes are apparent in Fig. 1b:

• The CO-poor régime in which P_{CO_2} changes linearly as a function of P_{CO}, with a proportionality factor around ≈0.1 weakly dependent upon the temperature. In this régime Low-Energy Electron Diffraction (LEED) characterization showed a (1 × 2) reconstructed pattern.[9]

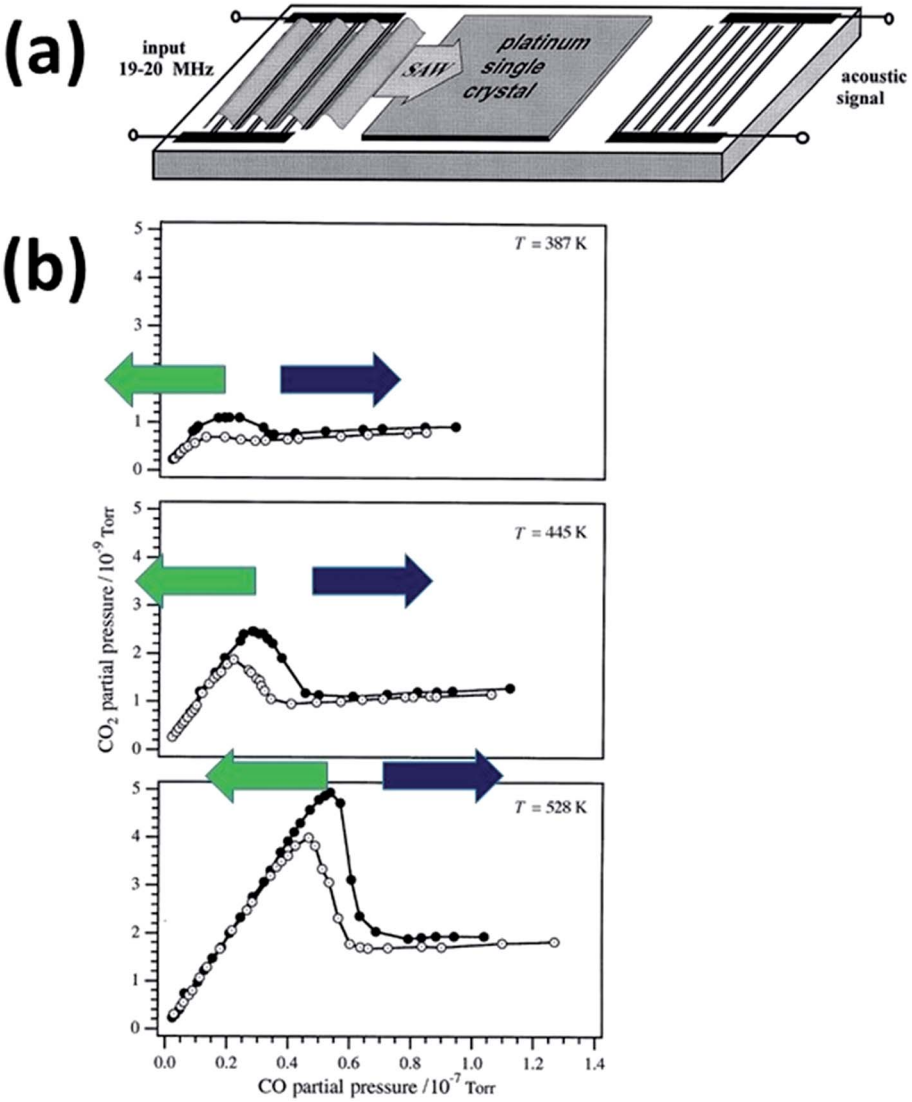

Fig. 1 (a) Schematic picture of the interdigital transducer device used by Kelling[6] to test the effect of SAW on heterogeneous catalysis. (b) Measurements of COox reaction rate: CO_2 partial pressure as a function of CO pressure with a constant baseline O_2 pressure $P_{O_2} = 1.2 \times 10^{-7}$ Torr at three different temperatures: from top to bottom in order of increasing temperature from $T = 387$, $T = 445$ and $T = 528$ K, and with SAW excitation off (white) or on (black). Green and blue arrows have been added to highlight the transition from CO-poor (green) to CO-rich (blue) régimes. Adapted with permission from ref. 6. © Royal Society of Chemistry (1997).

• The CO-rich régime for P_{CO} higher than a temperature-dependent threshold, where the COox reaction rate decreased dramatically, saturating at a plateau whose value also depends upon temperature. In these CO-rich conditions the (1×2) reconstruction of the Pt(110) surface is lifted. At CO coverages higher than ≈ 0.20 monolayers (ML, calculated relative to the density of Pt atoms in the (1×1) surface) the strong interaction of CO with Pt leads to the (1×1) unreconstructed surface.[9,10]

• The transition from the linear to the plateau régime of COox occurs when P_{CO} is large enough that the CO coverage exceeds ≈ 0.2 ML.

When the SAWs are turned on, the above qualitative picture does not change, however the SAW increases the P_{CO} threshold at which the cross-over to a pressure-independent régime occurs by roughly 20%. That is, the SAW extends the high-efficiency non-oscillatory linear régime by 20% (together with a weak increase in the P_{CO_2} plateau for the CO-rich region). Thus the effect of SAW on COox/Pt(110) is homologous to increasing the temperature of the transition by ≈ 35 K. However the experiments were carefully conducted to exclude any significant increase in the sample temperature under the given conditions (upper bound of <5 K), thus leaving open the question of the origin of the SAW-induced catalytic enhancement.

To gain insight into the atomistic mechanisms of these effects, we focused on the high-efficiency, O_2-rich or CO-poor branch of the COox reaction. Experimentally the bare Pt(110) surface exhibits the well-known (1×2) missing row reconstruction, formed by erasing every second topmost $[1\bar{1}0]$ row of Pt atoms.[16] This reconstruction is preserved under O_2-rich conditions[17] in which the surface is covered with O adatoms, as

schematically depicted in Fig. 2a for the Pt(110) surface with an oxygen-coverage of 1 ML (a CO molecule adsorbed on top of Pt rows is also shown in this figure). Note that the O adatoms are located in bridge/hollow sites of the fcc(111)-like facets that characterize the Pt(110) reconstructed surface.[18] For temperature in the range 387 to 528 K and $P_{O_2} = 1.2 \times 10^{-7}$ Torr the actual oxygen coverage is ~0.85 ML.[19] Thus we consider that a Pt(110) (3 × 2) cell with one O adatom missing represents a realistic model of Pt(110) at an O-coverage = 0.83 ML as shown in Fig. 2b. Under static long-time conditions and higher P_{O_2}, the O adatoms self-organize into a (11 × 2) 0.91 ML superstructure[17] that is weakly favorable thermodynamically.[20] But we expect that this ordered structure does not occur under the disordering influence of CO. Other quantities that will be used in the following are:

• Under the above conditions the experimental dissociative sticking probability for O_2 molecule onto Pt(110) is ~0.03 {Fig. 1 of ref. 21}.

• In contrast the dissociative sticking probability of O_2 onto the bare (1 × 2)-reconstructed Pt(110) surface at T around 500 K is ≈0.3 (see Fig. 2 of ref. 22).

• The CO sticking coefficient onto the bare (1 × 2)-reconstructed Pt(110) surface is about 0.6.[22]

We also calculated the NEB energy barrier for O-hole diffusion to be 0.88 eV at 0.83 ML coverage. Thus an O-adatom can jump from one site to the next will take place in 3×10^{-4} s at T = 528 K, implying that O-adatom diffusion is fast in these conditions.

We next investigated CO interaction with the Pt(110)-(1 × 2) at various O-coverages. At 1 ML O-coverage we find that CO adsorbs on-top of the ridge of [1$\bar{1}$0] rows (see Fig. 2a for a schematic depiction) with a very weak absorption enthalpy of 0.1 eV, so very little CO is on the ridge at ~500 K. We anticipate that our DFT results as reported below are in general consistent with both experiment and previous theoretical results.[20,23] However, one important difference we find with respect to previous computational studies is for the Eley–Rideal (ER) mechanism (the process in which a CO molecule hits a 1 ML-O-covered reconstructed Pt(110) surface and picks up an O adatom thus producing CO_2). To investigate this process in detail, we carried out the following calculations:

• We established an upper bound of 0.55 eV for the ER barrier, by carrying out NEB calculations along a path between an initial state in which CO is adsorbed on top of a [1$\bar{1}$0] ridge and a final state corresponding to the 0.83 ML-covered Pt(110) surface plus gas-phase CO_2 (as illustrated in Fig. 2c).

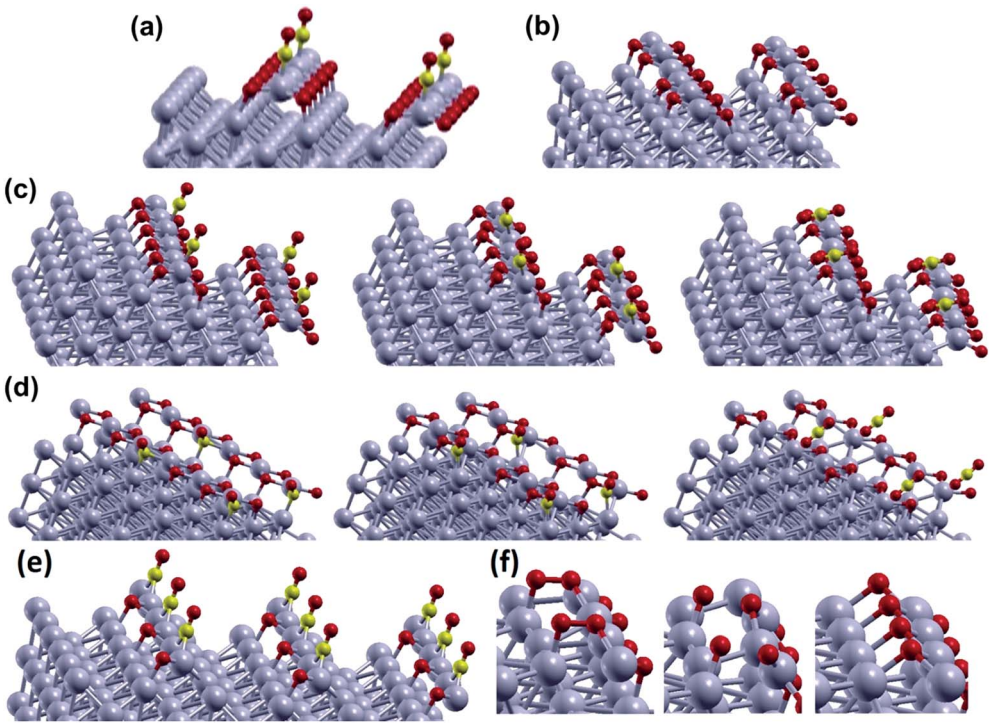

Fig. 2 (a–d) Schematic pictures of a reconstructed Pt(110) surface in various conditions for a (3 × 2) unit cell. (e and f) Same for the (2 × 2) cell. (a) 1 ML O-coverage with an additional CO molecule adsorbed on-top of the ridge of [1$\bar{1}$0] rows; (b) 0.83 ML O-coverage; (c) COox reaction occurring *via* a ER mechanism at 1 ML O-coverage with a CO molecule starting on-top of the ridge of [1$\bar{1}$0] rows (left-hand-most image), then in the saddle point of the reaction (middle image) and finally evolving CO_2 (right-hand-most image); (d) a COox reaction occurring *via* a LH mechanism at 0.83 ML O-coverage with a CO molecule starting on a (111)-like facet (left-hand-most image), then in the saddle point of the reaction (middle image) and finally evolving CO_2 (right-hand-most image); (e) CO adsorption on-top of the ridge of [1$\bar{1}$0] row far from O-adatoms at 0.25 ML O-coverage; (f) O_2 dissociation at 0.5 ML O-coverage starting from adsorption on a fcc(111)-like facet in the presence of two adjacent empty sites, going through a saddle point, and producing two nearest-neighbor O-adatoms, as illustrated in the left-hand-side, middle and right-hand-side, respectively. The (3 × 2) and (2 × 2) cells are replicated 4 times for clarity of illustration.

• For COox at 1 ML O-coverage, we carried out a systematic scan of the potential energy surface to find an energy barrier for ER of ≈0.4 to 0.5 eV, depending on the CO path.

• In contrast, Pedersen predicted a high (>1.1 eV) energy barrier for this process.[20]

A second difference we find with respect to previous theoretical studies is that

• We predict an even smaller COox barrier (≈0.3 eV) for an ER mechanism at low (0.25 ML) O-coverage. This is consistent with the most recent experimental evidence for COox on Pt(111), according to which the COox reactivity increases in the order: α-PtO_2 < Pt–O surface oxide [similar to 1 ML O-covered Pt(110)] < single O adatom.[24]

• In contrast, the previously predicted the lowest COox energy barrier was only 0.3 eV for the PtO_2 [10$\bar{1}$0] oxide phase,[20] which is not consistent with the experiments in which the COox barrier is smaller at low O-coverage.

At 0.83 ML O-coverage, we find that CO adsorbs on top of a [1$\bar{1}$0] row ridge next to the O-hole with an absorption energy of 0.53 eV, but we find that it is much more favorable (an adsorption energy of 1.52 eV) to adsorb in the hollow fcc(111)-like site left empty by the missing O adatom, as illustrated in the left-hand-side of Fig. 2d. In this site, CO can react with an adjacent O adatom to produce CO_2 *via* a Langmuir–Hinshelwood (LH) mechanism, a process illustrated in Fig. 2d. This decreases the total energy by 0.62 eV, leading to an energy barrier of 1.34 eV and an Arrhenius prefactor of 1.06×10^{13} Hz.

The value of 1.34 eV that we calculate for the energy barrier for COox in the LH path at 0.83 ML O-coverage is close to the value of the barrier for CO desorption (1.52 eV). We explain this as due to the repulsion between CO and adsorbed O-atoms that we find in this system. The small difference between the CO adsorption energy and the LH COox energy barrier (0.18 eV) suggests that the COox/Pt(110) reaction is dominated by a competition between these two different processes for the experimental conditions of interest (see the discussion below). The ER and LH mechanisms are both viable under the given conditions, however the ER mechanism has a much lower energy barrier (<0.5 eV) than the LH barrier (1.3 eV) while LH is favored by low pressure (low impinging rate). We note that CO_2 adsorption on Pt(110) at various O-coverages has been tested and found to be unfavorable with respect to CO_2 evolution, so that no formation of CO_2 nor CO_3 (carbonate) adsorbed species is expected, a result quite different for other metal heterogeneous catalysts.[25]

The picture emerging from these calculations is in excellent agreement with precise spectroscopic experimental characterization under reaction conditions,[26] which show the existence of two régimes for COox:

• A low-P_{CO}/high-rate branch where the reacting CO species is adsorbed on the Pt surface and embedded within an O-rich environment (it was proved experimentally that bridging CO is absent) of fully developed Pt oxides or subsurface oxygen.

• And a high-P_{CO}/low-rate branch.

At low O-coverage (or high CO coverage) the energy landscape for CO adsorption changes again. First, as mentioned above, the ER COox barrier drops to ≈0.3 eV at 0.25 ML O-coverage. Concurrently, CO adsorption changes both the site and energetics: as illustrated schematically in Fig. 2e, the CO adsorption energy is 1.77 eV at the on-top site of the ridge of [1$\bar{1}$0] rows, far from the O adatom. This strongly non-linear dependence of the CO + O energetics on the Pt(110) surface observed experimentally is expected since it is ultimately the origin of well-known oscillatory behavior of the COox process on this heterogeneous catalyst.[8]

Finally, our calculations show that O_2 dissociation on the reconstructed surface occurs only when two adjacent sites are empty (in agreement with previous studies[23]). In this case the O_2 molecule binds with an adsorption energy of 0.72 eV, and goes through a saddle point with an energy barrier of 0.54 eV to form O-adatoms at two nearest-neighbor sites, as illustrated schematically in the left-hand-side, middle and right-hand-side, respectively, of Fig. 2f for a (2 × 2) unit cell at 0.5 ML O-coverage. In contrast, in the absence of two adjacent vacant sites the probability of O_2 dissociation is negligible,[23] in agreement with experiment.[19]

For convenience of the reader, we summarize the results of static DFT calculations in Fig. S3 and S4 of the ESI.†

3.2 SAW-induced catalytic effects

Having clarified the energy landscape of CO over O-covered Pt(110)-(1 × 2) surface from static DFT calculations, we now explore how SAW-induced effects can affect the catalytic rates.

SAWs produce a homogeneous strain of the Pt lattice, as determined by Doppler experiments.[27] However in agreement with previous studies[28] we calculate that a sizable strain (of the order of 1–2%) is necessary to induce sufficiently large changes in adsorption energetics to influence catalytic rates. This strain is 100 times larger than observed for homogeneous SAW modulations of the surface (of the order of 10^{-4}, as noted above).

Also in agreement with previous studies[29] we find that electric fields of the order of a few V nm^{-1} would be necessary to change the adsorption and reaction energetics sufficiently to explain the observed increase in catalytic efficiency. For example, we calculate that an electric field of 1 V nm^{-1} changes the CO adsorption energy on Pt(110) by 0.015 eV. This suggests that a field of at least 6 V nm^{-1} would be required to produce a sizable effect of 0.09 eV. Such high electric fields are not expected under the SAW conditions, since many unobserved phenomena would be triggered at much lower field values.[30] Moreover such fields are unrealistic considering the thickness and screening of the Pt metallic layer, which would attenuate the electric field down to values ~1000 times smaller than required.[6]

The effects of SAW-induced homogeneous strain on diffusion[31] can also be excluded as well as the major cause of the observed increase in COox efficiency, since the diffusion energy barriers are also sizable (the barrier to O-diffusion is 0.88 eV) and thus appreciably modified only by much larger values of the strain.

The presence of structural defects might enhance SAW effects, but which kind of defects? Local defects are not visible

in PEEM experiments[6] in the low-*P*(CO), highly efficient, linear-régime branch of COox reaction. An interesting hint comes from the observation that the SAW-enhanced catalysis does not occur on the pristine sample, but only after an incubation time.[6] A more thorough characterization[27] ascertained that during the incubation time the surface begins to exhibit damage, with the Pt layers developing cracks, while Pt-species down to single Pt atoms are scattered away from the damaged surface onto the surrounding of the sample. In particular, a model for generating cracks by phase shift of the acoustic waves was proposed, in which sudden "spikes" or "riggles" develop at the surface of the Pt layer due to interference of SAW. This effect is similar to that of shock wave that we investigated previously in a different context.[32]

To obtain information about the atomistic processes produced by a shock wave at the Pt(110) surface, we constructed a model Pt(110) 17 nm-thick slab (7170 atoms) and used the ReaxFF reactive force field[33] with parameters specifically derived for Pt systems[34] to investigate the impact of this slab against a hard wall. Snapshots and the velocity distribution from this simulation in Fig. S1† and 3 show the effects of a shock wave generated at one end of the slab as it propagates through the slab to reflect off the opposite free (110) surface. We observe that the impinging wave produces a temporary flattening of the surface as one most notable effect. To translate this result into a first-principles AIMD dynamics simulation of a reactive system, we devised the following computational procedure:

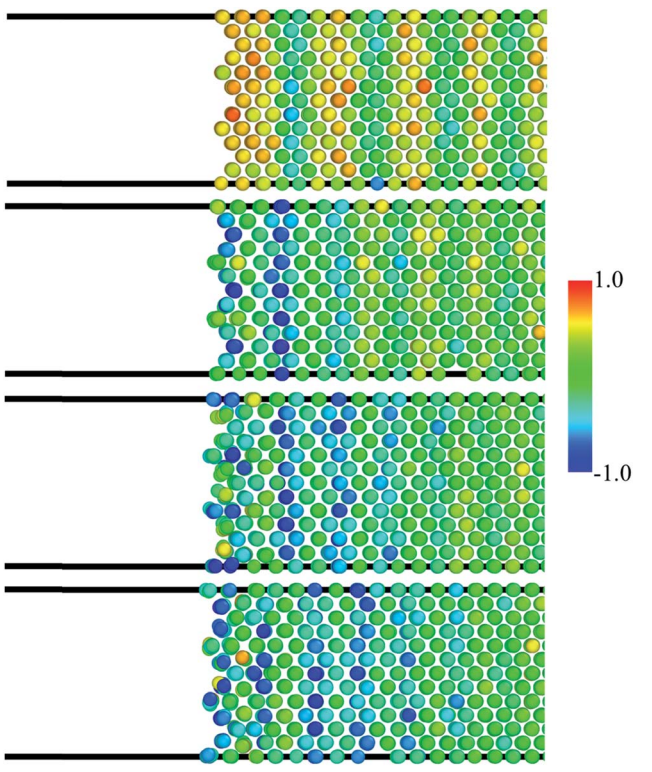

Fig. 3 Positions and velocity distribution along shock direction (V_z component) for the atoms near the free surface from ReaxFF simulations of the collision of a Pt(110) slab against a hard wall positioned at extreme right-hand-side of the picture (see also Fig. S1†). Each snapshot captures the systems at increasing times from top to bottom. The times are 3.4, 3.9, 4.1, 4.2 ps from top to bottom [color coding for velocity distribution (unit: km s^{-1})].

- We took a (3 × 2) cell of a 0.88 nm-thick Pt(110) slab covered on one side by co-adsorbed CO and O. Here we used 1 adsorbed CO molecule and 5 O adatoms (0.83 ML O-coverage) as in the left-most panel of Fig. 2(d).
- We carried out *ab initio* molecular dynamics (AIMD) after first equilibrating the system at 300 K for 10 ps.
- Then to model the effect of phase-shifted SAW we extended the two bottom Pt layers by 0.5 Å from the rest of the system (as suggested by the ReaxFF shock wave simulations in Fig. 3), fixed them, and carried out a final NVE AIMD calculation at a temperature of 1700 K (since AIMD simulations can only be done for few ps, a high temperature is needed to observe dynamic phenomena).

We find that without SAW no reactive event is observed on the equilibrated CO & O-covered Pt(110) surface over the period of 10 ps, even at this high temperature. However with the SAW we observed that several dynamic processes are triggered in the AIMD simulations (a movie of a representative trajectory is included in the ESI†). The temperature and the internal energy changes of the system under SAW conditions are displayed in Fig. S2,† and show an increase in the temperature by ≈300 K due to SAW shock wave. Here we see:

- CO diffusion (also in the form of a Pt–CO unit as illustrated in Fig. 4a). This occurred 4 times in the 7 simulations.
- Pt–CO detachment (Fig. 4b). This occurred in 5 of the 7 simulations.
- COox reaction (Fig. 4c and the ESI movie†). This occurred in 3 of the 7 simulations.

These simulations provide a rational for the experimentally observation.

First, CO diffusion is found to be facile, both as a CO molecule and as a Pt–CO unit, as illustrated in Fig. 4a. In particular, CO interacts strongly with the less coordinated Pt atoms so that a Pt–CO unit rather than a single CO molecule can sometimes desorb from the surface. We note in this connection that our computational approach predicts an adsorption energy of 2.0 eV for CO on top of a ridge of the bare reconstructed Pt(110) surface at zero O-coverage. This value is in very good agreement with the 1.9 eV estimate from calorimetric experiments in the limit of low coverage (see Fig. 1 in ref. 22) but is much larger than the estimate of 1.56 eV from surface temperature[35] and molecular beam modulation[36] techniques. This discrepancy can be reconciled by noting that the CO molecule in the pre-desorption state acquires a significant entropic free-energy component from libration modes, a component that is absent in the equilibrium configuration. From a previous analysis[37] we derive that this increases the Arrhenius prefactor of CO desorption by a factor $\approx 10^2$ with respect to values typical for surface processes. Indeed in ref. 37 the desorption of CO from a Ni(110) surface was considered. Using a classical stochastic diffusion equation for the distance between the C atom and the surface and assuming that the adsorbed CO molecule can transform energy from the bending (librational) mode of the O atom about the Ni–C bond into translational kinetic energy, an Arrhenius expression for the rate

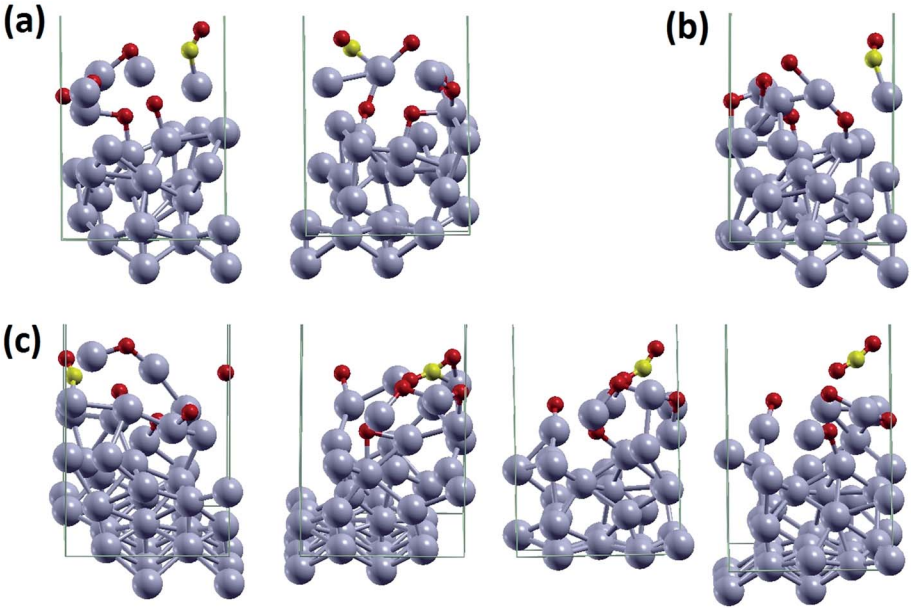

Fig. 4 Snapshots from AIMD simulations illustrating the dynamic processes thereby extracted: (a) CO diffusion (also in the form of a Pt–CO unit); (b) Pt–CO detachment; (c) COox reaction.

of CO desorption was obtained differing from a standard one only in the pre-exponential factor which turned out to be $\approx 10^{15}$ instead of $\approx 10^{13}$ as predicted from the characteristic frequency of the adsorbate–surface interaction potential. The increase in librational entropy singled out in the CO-over-Ni(110) case is typical for CO desorption. Thus, we use the same estimated number for our CO-over-Pt(110). This produces an apparent decrease of the CO adsorption energy under dynamic condition that is not expected in static experiments such as temperature-stimulated desorption experiments. This point (usually neglected in the analysis of these experiments *via* the Redhead equation) will be important in the kinetic analysis below.

Second, we observe detachment of Pt in our simulations, not as a Pt atom but as the more stable Pt–CO unit (Fig. 4b). This rationalizes the experimental observation of Pt-species down to single Pt atoms scattered away from the damaged surface into the regions surrounding the sample.[6] This is thus qualitatively in agreement with the presence of stochastic spikes at the surface.

Third, the SAW-induced spikes in our AIMD simulations eventually promote COox reactions (Fig. 4c). Interestingly this occurs *via* an ER-like mechanism in which CO first shifts from (111)-facet adsorption to on-top $[1\bar{1}0]$ ridge adsorption, from which it descends back to the O-covered (111)-like surface to pick up an O adatom and produce gas-phase CO_2. This is similar to the results of our scan of the potential energy surface at the static DFT level for the ER COox mechanism (see above). This excellent agreement between static DFT and dynamic AIMD simulations corroborates both observations.

3.3 Kinetic model

We can now quantify our analysis. The highly efficient régime of the COox reaction is suppressed at high P(CO) by the competition between O_2 dissociation *vs.* CO adsorption sticking probabilities turning in favor of CO, which eventually covers and poisons the surface. We know from experiment[8] that the switch between low-P(CO) and high-P(CO) régimes occurs when CO-coverage is about 0.2 ML. We define the following simplified kinetic model:

$$\dot{g}_{CO} = g_e \times I_{CO} \times S_{CO} - g_{CO} \times [g_O \times R_{COox} + R_{des}] \quad (1)$$

$$\dot{g}_O = 2I_{O_2} \times \sqrt{(32/28)} \times S_{O_2}[g_e] - 2I_{O_2} \times \sqrt{(32/28)} \times S^0_{O_2} \times (g_O)^2 / (g^0_O)^2 - d[CO_2/dt] \quad (2)$$

$$\dot{g}_e = 2I_{O_2} \times \sqrt{(32/28)} \times S^0_{O_2} \times (g_O)^2 / (g^0_O)^2 - 2I_{O_2} \times \sqrt{(32/28)} \times S_{O_2}[g_e] - g_{CO} \times [2g_O \times R_{COox} + R_{des}] - g_e \times I_{CO} \times S_{CO} + S_{ER} \times I_{CO} \times g_{CO} \quad (3)$$

$$d[CO_2]/dt = S_{ER} \times I_{CO} \times g_O + g_{CO} \times g_O \times R_{COox} \quad (4)$$

where:

$$g_e = \text{coverage of empty sites in ML} \quad (5)$$

$$g_O = \text{coverage of O-adatoms in ML} \quad (6)$$

$$g^0_O = \text{O-coverage in the absence of CO} = 0.85 \text{ ML [ref. 19]} \quad (7)$$

$$g_{CO} = \text{coverage of CO in ML} \quad (8)$$

and the corresponding dotted $\dot{g}$-quantities represent time derivatives, while

$$I_{CO} = \text{impingement rate of CO} \quad (9)$$

$$I_{O_2} = \text{impingement rate of } O_2 \quad (10)$$

$$S_{CO} = \text{sticking coefficient of CO on an empty site} = 0.6 \text{ [ref. 22]} \quad (11)$$

$$S_{O_2}[g_e] = \text{dissociative sticking coefficient of } O_2 = 0.3 \text{ (ref. 22)} \times \{\text{probability of adjacent empty sites}\}[g_e] \quad (12)$$

$$\{\text{Probability of adjacent empty sites}\}[g_e] = 2[(n-1)/n] \times (g_e)^2 \times \{1 + (n-2)(n-3/2)/100\} \quad (13)$$

$$S^0_{O_2} = S_{O_2}[g_e] \text{ coefficient in the absence of CO} = 0.03 \text{ [ref. 21]} \quad (14)$$

$$S_{ER} = \text{probability of an Eley–Rideal COox reactive event} = 0.093 \quad (15)$$

$$R_{COox} = \text{COox LH reaction rate} = 1.06 \times 10^{13} \times \exp[-1.34 \text{ eV}/k_B T] \quad (16)$$

$$R_{des} = \text{CO desorption rate} = 100 \times 1.06 \times 10^{13} \times \exp[-1.52 \text{ eV}/k_B T] \quad (17)$$

$$d[CO_2]/dt = \text{rate of } CO_2 \text{ production} \quad (18)$$

where $n = g_e \times 100$, T is the temperature, k_B is the Boltzmann constant, and the {probability of adjacent empty sites} as a function of g_e is obtained by a binomial mathematical formula eqn (13) (expanded up to the fourth order in g_e).

Formula (13) predicts that in the absence of CO at $g^0_e = 1 - g^0_O = 0.15$ ML the probability of two empty adjacent sites is $\approx$0.116 so that $S_{O_2}[g_e] = 0.3 \times 0.116 \approx 0.03$ in keeping with experiment.[21]

Note that we have $\dot{g}_{CO} + \dot{g}_e + \dot{g}_O = 0$, as it should be since $g_{CO} + g_e + g_O = 1$.

The Eley–Rideal S_{ER} sticking coefficient is estimated as $\approx$0.093 to ensure consistency with experiment[21] and with the observed approximately linear behavior of the rate of CO_2 production as a function of P_{CO} in CO-poor conditions (see Fig. 1).

Some numbers derived from this analysis are as follows:

(1) The O_2 impingement rate I_{O_2} corresponds to one collision every 54 s per surface site at $P_{O_2} = 1.2 \times 10^{-7}$ Torr and $T = 528$ K. The rate of O_2 dissociation is obtained by multiplying this number times the dissociative sticking coefficient, which is about 0.03 at $g_e = 0.15$ ML (in the absence of CO).[21]

(2) The CO adsorption rate is given by the CO impingement rate (I_{CO}, related to the O_2 impingement rate times the ratio of pressures and the square root of mass ratio) times the sticking coefficient of CO onto an empty site (0.6 [ref. 6]) times the fraction of empty sites. This leads to ~one event every several 10^2 seconds per surface site under operating conditions.

(3) The rate for the COox reaction of adsorbed CO molecules is given in eqn (1)–(4) as the product of O-coverage times CO-coverage ($g_O \times g_{CO}$) times the COox LH reaction rate, which is determined by an Arrhenius formula with a prefactor (1.06×10^{13} Hz) and an activation energy (1.34 eV) as calculated at the DFT level (see above).

(4) The rate of CO desorption is instead determined by an Arrhenius formula with a prefactor calculated as 100 times the prefactor for LH COox[36] and a DFT-calculated activation energy (1.52 eV, see above).

Clearly the formula for the COox LH reaction rate [$=g_O \times g_{CO} \times R_{COox}$] holds for CO molecules adsorbed within an environment of O-adatoms as in Fig. 2c. This model is realistic as long as the rate of CO desorption and LH COox is slower than the CO adsorption rate, which under the given conditions is certainly true up to $T = 445$ K.

However at $T = 528$ K we find that CO desorption and LH COox become much faster (time-scale of seconds) than CO adsorption (time-scale of hundreds of seconds). This corresponds to a different régime in which CO would not poison the surface, because CO in the gas phase becomes thermodynamically more stable than CO adsorbed on the Pt(110) surface within an environment of O-adatoms. In such a régime, CO that was adsorbed on-top of the ridge of [1$\bar{1}$0] rows in the low O-coverage regions becomes the dominant species (see Fig. 2e), with an adsorption energy increasing from 1.52 eV (Fig. 2d, left-hand-side) to 1.77 eV (Fig. 2e). This is sufficiently large to stabilize it against CO in the gas phase. In this régime adsorbed CO will reorganize in patches or islands with a low O-coverage. From these different adsorption sites CO will jump onto a fcc(111)-like facet next to an O adatom to produce CO_2 *via* a LH mechanism. In a first approximation we take this into account in the kinetic model described above by assuming an equilibrium between CO on-top of [1$\bar{1}$0] ridges and CO next to an O-adatom, and then using the same kinetic formulae eqn (1)–(18) with R_{COox} and R_{des} modulated by the Boltzmann factor = exp [$-(1.77 - 1.52$ eV$)/k_B T$]. This will then be assumed in the following analysis.

Assuming now steady-state conditions we set: $\dot{g}_{CO} = \dot{g}_e = \dot{g}_O = 0$, and we solve the resulting eqn (1)–(3) subject to the constraint $g_{CO} + g_e + g_O = 1$. The solution is not analytic due to the presence of higher powers in the unknowns, but we obtained results numerically. To give a qualitative but realistic idea of the solution of this model, we note that, setting eqn (1) = 0, we obtain:

$$g_{CO} = g_e \times I_{CO} \times S_{CO}/[g_O \times R_{COox} + R_{des}] \quad (19)$$

Now, considering that g_O does not change much under the given conditions (ranging between 0.85 and 0.65 ML), formula (19) predicts that the number of surface sites covered by CO is simply proportional to the number of empty sites. Note that the coefficient of proportionality is basically given by the ratio between the rate of impingement *vs.* that of surface processes, where the quantities I_{CO}, S_{CO}, R_{COox}, R_{des}, are either constant or known as function of temperature and pressure, see formulae (9)–(18) above. The precise numerical solution of the kinetic model provides us with the following estimates.

At $P(O_2) = 1.2 \times 10^{-7}$ Torr and $T = 445$ K, we predict that $g_{CO} \approx 0.2$, and thus the predicted switch between low-P(CO) and high-P(CO) régimes, at $P_{CO} = 0.43 \times 10^{-7}$ Torr, which can be compared with the experimental value of 0.23×10^{-7} Torr.

At $P(O_2) = 1.2 \times 10^{-7}$ Torr and $T = 528$ K, we predict that $g_{CO} \approx 0.2$ at $P_{CO} = 0.73 \times 10^{-7}$ Torr, which can be compared with the experimental value of 0.45×10^{-7} Torr.

We also predict that the ratio between $P(CO_2)$ and $P(CO)$ in steady state is around 0.11 to 0.12, which is close to the experimental value of $\approx$0.1 (see Fig. 1).

Considering the approximations involved, the intrinsic uncertainties of DFT predictions, and the sensitivity of the system kinetics to variations in the input parameters, the proposed picture is at least semi-quantitatively consistent with experiment. Indeed, if we simply increase the value of the energy barrier for the COox LH reaction and CO desorption by 0.026 eV (*i.e.*, changing them from 1.34 eV to 1.366 eV and from 1.52 eV to 1.546 eV, respectively), we predict a P_{CO} threshold = 0.23×10^{-7} Torr at $T = 445$ K and = 0.424×10^{-7} Torr at $T = 528$ K, respectively, which match very well the experimental values of 0.23×10^{-7} Torr and 0.45×10^{-7} Torr, respectively.

We now consider the SAW case. The AIMD simulations suggest that turning on SAW activates several dynamic processes, as discussed above. It is not easy to quantify the corresponding effect on the CO oxidation process because the AIMD simulation must be run at elevated temperature to observe dynamic processes in the time scale of *ab initio* molecular dynamics (few ps), even in the presence of SAW excitation. Thus our statistics are necessarily limited by the computational effort associated with AIMD simulations. Moreover processes such as Pt–CO desorption generates fresh new catalyst surface that can drastically change the energy landscape of the reaction. Nevertheless, the present findings can be summarized as follows.

• First, we do not observe any reactive or desorption processes during the 10 ps AIMD control runs in the absence of SAW stimulation.

• Second, considering all the AIMD NVE runs (*i.e.*, for a total simulation time of 25 ps) we observe 3 LH COox events, 4 CO desorption events, and 1 Pt–CO desorption event. Here the time scales of LH COox and desorption are different: CO or Pt–CO desorption occur on average within the first 1.8 ps, whereas LH COox events occur on average after 4.3 ps. In other words, the first effect of the SAW spike is to desorb CO with high probability. However, even if the spike does not succeed in desorbing CO in the first 1.8 ps, the energy lingering in the system (recall that we conduct NVE simulations) can promote LH COox reaction with a probability of about 40–50% after 4.3 ps.

To translate these observations into quantitative estimates of the effect of SAW on the efficiency of the COox catalytic process, we consider for simplicity only the SAW increase in CO desorption. The total area of the catalyst used in the experiment is 0.4×0.4 mm^2[9] which (at $g_{CO} \approx 0.2$) corresponds to $\approx 3 \times 10^{11}$ surface sites. Each SAW cycle occurs with a frequency around 20 MHz, which we assume may produce several shock events. If we assume that each SAW cycle produces – say – 7 CO desorption events over the whole area of the catalyst, this will increase the CO desorption rate by $\approx$20%. Thus the ratio of surface processes $[g_O \times R_{COox} + R_{des}]$ with respect to the CO impingement rate in eqn (19) will shift the P_{CO} threshold at which the switch between low-P(CO) and high-P(CO) régimes occurs. In particular, assuming 7 CO desorption events per SAW cycle, the switch between the two régimes in the presence of SAW stimulation is predicted to occur for

• $P(CO) = 0.30 \times 10^{-7}$ Torr when $T = 445$ K and
• $P(CO) = 0.51 \times 10^{-7}$ Torr when $T = 528$ K, respectively.

This can be compared to the experimental values of

• $P(CO) = 0.29 \times 10^{-7}$ Torr when $T = 445$ K and
• $P(CO) = 0.54 \times 10^{-7}$ Torr when $T = 528$ K.

Thus, despite the several approximations involved in the present analysis and uncertainties in predicted energetics, we conclude that our proposed mechanism is in semi-quantitative agreement with experiment, thus providing a consistent atomistic mechanistic understanding and rationalization.

4. Conclusions and perspectives

In summary, we present here a QM-based theoretical analysis and assessment of the experimentally observed surface-acoustic-wave (SAW)-induced enhancement of the COox/Pt(110) reaction.[6,9,27] Our AIMD simulations lead to atomistic mechanisms for SAW to enhance such dynamic processes as diffusion, desorption, and reaction, that are accelerated by the several short shocks during each cycle of the SAW. This spectrum of SAW induced fluctuations in the surface concentrations indicates a decoupling of the degrees of freedom related to space and velocity that is qualitatively different from that of thermal fluctuations. That is, the SAW can increase fluctuations in localized regions of space while keeping fluctuations in velocity averaged over large distances basically constant.

This development of an atomic mechanism is a necessary step to start exploiting the SAW approach to modulate and control surface effects. We find that short picosecond shocks from domain flipping transitions during the SAW 20MHx cycle provide the possibility of delivering localized packets of energy to specific, performance-limiting mechanistic steps (in the present case the desorption of the CO poisoning species) to provide a novel means to affect local atomistic level modulations that can alter catalytic rates. This mechanism provides a basis for selecting other catalyst processes that might be dramatically enhanced with SAW.

For example, we considered here a continuous film deposited on the piezoelectric surface. However, this should apply equally for polycrystalline samples as those used in Inoue's experiments[5] provided that there are pathways for the shock to propagate to the catalytic surface. To extend this concept to such high surface area materials as catalyst nanoparticles on inactive porous supports, it would be important to ensure that the shock propagation can proceed from the piezoelectric surface to the catalyst surface. Highly anisotropic materials seem especially appealing in this respect.

However, a major challenge in making this AWEC approach effective will be to achieve precise control of AW-induced dynamical processes, that avoids dispersion of SAW energy into purely thermal dissipation or (worse) unwanted side-processes such as scattering of Pt atoms as in the COox/Pt(110) case here investigated. One intriguing possibility in this respect might be surface nanopatterning *via* deposition of size-selected

nanoclusters from the gas phase that might control the grain size, morphology, and boundaries to focus and control the shocks at the catalytic surfaces.

Acknowledgements

This work was funded by the U.S. Department of Energy's Advanced Research Projects Agency-Energy (ARPA-E) under contract number DE-AR0000552.

References

1 C. Marcilly, *J. Catal.*, 2003, **216**, 47–62.
2 J. N. Galloway, F. J. Dentener, D. G. Capone, E. W. Boyer, *et al.*, *Biogeochemistry*, 2004, **70**, 153–226.
3 A. Assion, T. Baumert, M. Bergt, T. Brixner, B. Kiefer, V. Seyfried, M. Strehle and G. Gerber, *Science*, 1998, **282**, 919–922.
4 B. J. Sussman, D. Townsend, M. Y. Ivanov and A. Stolow, *Science*, 2006, **314**, 278–281.
5 Y. Inoue, *Surf. Sci. Rep.*, 2007, **62**, 305–336.
6 S. Kelling, T. Mitrelias, Y. Matsumoto, V. P. Ostanin and D. A. King, *Faraday Discuss.*, 1997, **107**, 435–444.
7 S. J. Reese, D. H. Hurley and H. W. Rollins, *Ultrason. Sonochem.*, 2006, **13**, 283–286.
8 R. Imbihl and G. Ertl, *Chem. Rev.*, 1995, **95**, 697–733.
9 S. Kelling, S. Cerasari, H. H. Rotermund, G. Ertl and D. A. King, *Chem. Phys. Lett.*, 1998, **293**, 325–330.
10 T. Gritsch, D. Coulman, R. J. Behm and G. Ertl, *Phys. Rev. Lett.*, 1989, **63**, 1086–1089.
11 J. P. Perdew, K. Burke and M. Ernzerhof, *Phys. Rev. Lett.*, 1996, **77**, 3865–3868.
12 P. E. Blöchl, *Phys. Rev. B: Condens. Matter Mater. Phys.*, 1994, **50**, 17953–17978.
13 P. Giannozzi, S. Baroni, N. Bonini, M. Calandra, R. Car, C. Cavazzoni, D. Ceresoli, G. Chiarotti, M. Cococcioni, I. Dabo, *et al.*, *J. Phys.: Condens. Matter*, 2009, **21**, 395502.
14 G. Henkelman, B. P. Uberuaga and H. Jónsson, *J. Chem. Phys.*, 2000, **113**, 9901–9904.
15 G. Kresse and J. Furthmüller, *Phys. Rev. B: Condens. Matter Mater. Phys.*, 1996, **54**, 11169–11186.
16 A. M. Lahee, W. Allison, R. F. Willis and K. H. Reider, *Surf. Sci.*, 1983, **126**, 654–660.
17 S. Helveg, W. X. Li, N. C. Bartelt, S. Horch, E. Lægsgaard, B. Hammer and F. Besenbacher, *Phys. Rev. Lett.*, 2007, **98**, 115501.
18 G. Binnig, H. Rohrer, C. Gerber and E. Weibel, *Surf. Sci.*, 1983, **131**, L379–L384.
19 N. Freyer, M. Kiskinova, G. Pirug and H. P. Bonzel, *Surf. Sci.*, 1986, **166**, 206–220.
20 T. M. Pedersen, W. X. Li and B. Hammer, *Phys. Chem. Chem. Phys.*, 2006, **8**, 1566–1574.
21 A. V. Walker, B. Kloetzer and D. A. King, *J. Chem. Phys.*, 1998, **109**, 6879–6888.
22 C. E. Wartnaby, A. Stuck and Y. Y. Yeo, *J. Phys. Chem.*, 1996, **100**, 12483–12488.
23 T. Zhu, S.-G. Sun, R. A. van Santen and E. J. M. Hensen, *J. Phys. Chem. C*, 2013, **117**, 11251–11257.
24 D. Miller, H. S. Casalongue, H. Bluhm, H. Ogasawara, A. Nilsson and S. Kaya, *J. Am. Chem. Soc.*, 2014, **136**, 6340–6347.
25 F. R. Negreiros, L. Sementa, G. Barcaro, S. Vajda, E. Aprà and A. Fortunelli, *ACS Catal.*, 2013, **2**, 1860–1864.
26 J. H. Miners, S. Cerasari, V. Efstathiou, M. Kim and D. P. Woodruff, *J. Chem. Phys.*, 2002, **117**, 885–896.
27 S. Kelling, N. Saito, Y. Inoue and D. A. King, *Appl. Surf. Sci.*, 1999, **150**, 47–57.
28 M. W. Wu and H. Metiu, *J. Chem. Phys.*, 2000, **113**, 1177–1183.
29 N. Bonnet, I. Dabo and N. Marzari, *Electrochim. Acta*, 2014, **121**, 210–214.
30 W. Steurer, S. Surnev, F. P. Netzer, L. Sementa, F. R. Negreiros, G. Barcaro, N. Durante and A. Fortunelli, *Nanoscale*, 2014, **6**, 10589–10595.
31 A. Cut, V. Y. Zaitsev and L. V. Zhigilei, *J. Phys. Chem. C*, 2013, **117**, 9252–9258.
32 Q. An, S. V. Zybin, W. A. Goddard III, A. Jaramillo-Botero, M. Blanco and S.-N. Luo, *Phys. Rev. B: Condens. Matter Mater. Phys.*, 2011, **84**, 220101.
33 A. C. T. van Duin, S. Dasgupta, F. Lorant and W. A. Goddard III, *J. Phys. Chem. A*, 2001, **105**, 9396–9409.
34 C. F. Sanz-Navarro, P. O. Astrand, D. Chen, M. Ronning, A. C. T. van Duin, T. Jacob and W. A. Goddard III, *J. Phys. Chem. A*, 2008, **112**, 1392–1402.
35 J. R. Engstrom and W. H. Weinberg, *Surf. Sci.*, 1998, **201**, 145–170.
36 J. Fair and R. J. Madix, *J. Chem. Phys.*, 1980, **73**, 3480.
37 A. Redondo, Y. Zeiri and W. A. Goddard III, *Phys. Rev. Lett.*, 1982, **49**, 1847–1850.